

## NANOPARTICLES

# Spontaneous weathering of natural minerals in charged water microdroplets forms nanomaterials

B. K. Spoorthi<sup>1</sup>, Koyendrila Debnath<sup>2</sup>, Pallab Basuri<sup>1</sup>, Ankit Nagar<sup>1</sup>, Umesh V. Waghmare<sup>2</sup>, Thalappil Pradeep<sup>1,3\*</sup>

In this work, we show that particles of common minerals break down spontaneously to form nanoparticles in charged water microdroplets within milliseconds. We transformed micron-sized natural minerals like quartz and ruby into 5- to 10-nanometer particles when integrated into aqueous microdroplets generated via electrospray. We deposited the droplets on a substrate, which allowed nanoparticle characterization. We determined through simulations that quartz undergoes proton-induced slip, especially when reduced in size and exposed to an electric field. This leads to particle scission and the formation of silicate fragments, which we confirmed with mass spectrometry. This rapid weathering process may be important for soil formation, given the prevalence of charged aerosols in the atmosphere.

**N**anoparticles of minerals exist naturally in soil, and some of them are essential for life (1). Microdroplets have been a topic of interest over the past decade, and the confined environment within them is known to cause chemical synthesis at an accelerated rate, as well as other processes such as the formation of nanoparticles (2). We decided to explore whether natural minerals could disintegrate in microdroplets, through a process opposite to chemical synthesis.

For our experiments, we prepared micron-scale particles of natural quartz ( $\text{SiO}_2$ ) and ruby ( $\text{Cr}$ -substituted  $\text{Al}_2\text{O}_3$ ) for use in an electrospray setup (Fig. 1, A and B). We ground commercial millimeter-sized quartz particles well using a

mortar and pestle and used centrifugation to separate the differently sized particles that formed. We carefully excluded all the particles smaller than 1  $\mu\text{m}$  in size and used particles of 5 to 10  $\mu\text{m}$  that were suspended in water for the experiment (Fig. 1C). Even after ultrasonication to detach any adhered particles, we found some smaller particles attached to a few larger ones (Fig. 1C). These adhering particles had dimensions greater than 100 nm (fig. S1). We took an optical image of the ground quartz powder and an optical microscopic image of the separated particles that we used for electrospray (fig. S2). We electrosprayed a suspension of about 0.1 mg/ml of the separated quartz particles through a capillary

tube that had an inner diameter of 50  $\mu\text{m}$  at a flow rate of 0.5 ml/hour and observed the resulting plume (Fig. 1A). We collected the product of electrospray 1.5 cm away from the spray tip, which resulted in a flight time on the order of 10 ms, consistent with similar experiments (3, 4). The product that was deposited on a transmission electron microscopy (TEM) grid had only 5- to 10-nm-diameter particles (Fig. 1D) throughout the grid. Under higher magnification, particles of different morphologies were observed. The particles showed the (110) plane of quartz (inset of Fig. 1D). Sonication had no effect on the breaking of silica particles. Experimental methods are presented in the supplementary materials, including a video of the electrospray process (movie S1).

To ensure that our initial observations were truly representative of the process, we performed measurements on larger quantities of samples. We built a multinozzle electrospray unit composed of six nozzles. We electrosprayed 1 liter of the suspension that contained 100 mg of the crushed micron-sized particles discontinuously over a month at the optimized conditions (spray voltage and distance) and a 3 ml/hour flow rate, and a deposit

<sup>1</sup>Department of Chemistry, Indian Institute of Technology Madras, Chennai 600036, India. <sup>2</sup>Theoretical Sciences Unit, Jawaharlal Nehru Centre for Advanced Scientific Research, Bangalore 560064, India. <sup>3</sup>International Centre for Clean Water, IIT Madras Research Park, Chennai 600113, India.

\*Corresponding author. Email: pradeep@iitm.ac.in

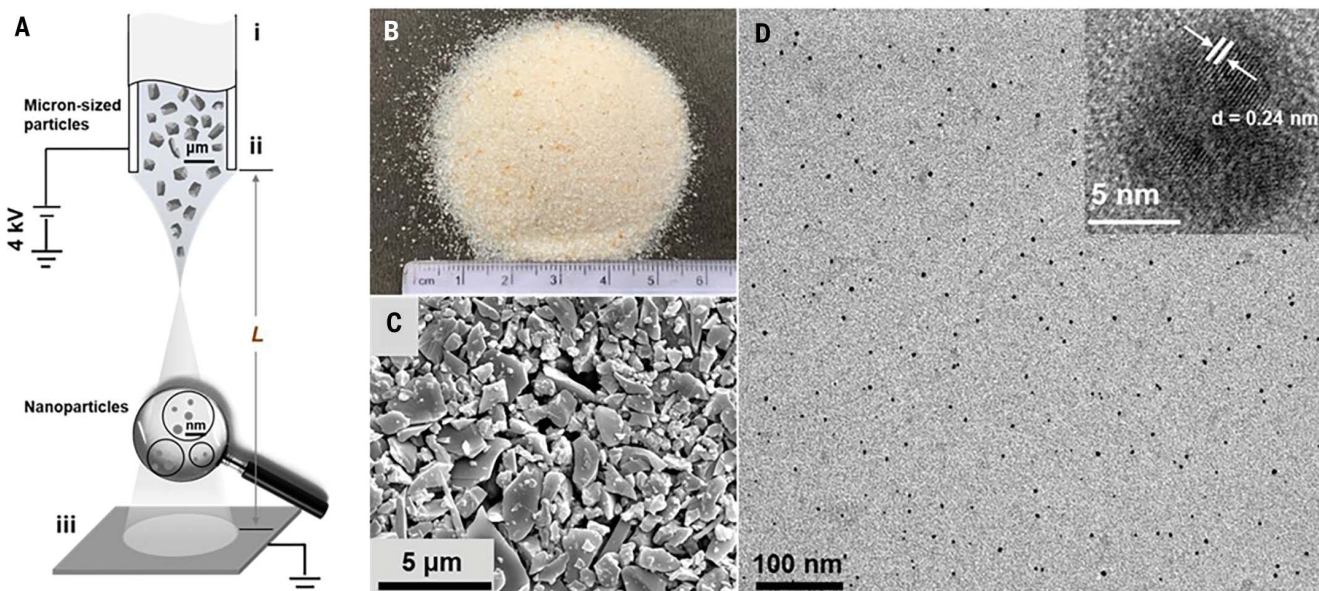


**Fig. 1. Process of disintegration of natural quartz in microdroplets.**

(A) Schematic representation of the disintegration of mineral particles in microdroplets. Setup components include (i) the electrospray emitter, (ii) a spray capillary with a 50- $\mu\text{m}$  inner diameter, and (iii) the conducting substrate at a distance of  $L = 1.5$  cm from the tip of the emitter. (B) A photograph of the natural quartz. (C) Field-emission scanning electron microscopy (FESEM) image of

ground and separated natural quartz used for electrospray, showing that the size range of particles is between 1 and 5  $\mu\text{m}$ . A few smaller particles that are naturally adhered to the micron-sized particles remain attached even after ultrasonication. (D) TEM image of natural quartz after electrospray with a high-resolution image of a particle shown in the inset. The plane shown is (110), where  $d$  is lattice spacing.

was collected on an aluminum sheet. The electrospray-deposited particles were strongly adherent to the substrate. We scraped about 60 mg of the powder off the substrate for bulk analysis. This left about 20 mg on the substrate, which we determined gravimetrically. We avoided hard scratching to remove the remaining product on the substrate. This gave us a collection efficiency of ~80% for our electrospray setup. We made x-ray diffraction measurements of the scraped-off powder using Cu K $\alpha$  radiation to confirm that it was made of quartz (fig. S3) in the form of nanoparticles of ~16-nm average diameter. We calculated the particle size using the Scherrer formula. Independent analysis, the details of which are presented in the supplementary materials, showed the collection yield of electrospray deposition to be 81%.

We obtained similar experimental results with ruby (Fig. 2, A to C) and fused alumina (Fig. 2, D to F). These experiments show that both natural minerals and their synthetic analogs can be fragmented in charged microdroplets. The synthesis of materials using electrospray requires optimized conditions (5). For our single-spray experiments, the electro-

spray voltage was 4.0 kV, the tip-to-collector distance was 1.5 cm, and particle loading was 0.1 mg/ml.

#### Optimized experimental parameters

In the case of silica, below a spray voltage of 2.5 kV, the spray did not occur. From 3.0 kV onward, the spray was uniform. This potential was the threshold at which the electric field breaks the limit of surface tension and forms a plume containing charged microdroplets from the tip of the emitter. The required potential for this varies for different solutions and suspensions. In our experiments, the threshold potential for a stable spray was higher than usual, mainly because we electrosprayed a fine suspension of quartz. Below 2.5 kV, only micron-sized particles were seen in the outcome. We observed maximum fragmentation at the optimized conditions. Particles fragmented well at 4.5 kV. At 5.5 kV, we even observed finer nanostructures (fig. S4). We characterized the samples before and after electrospray by Raman spectroscopy (fig. S5) and energy dispersive spectroscopy. We observed fragmentation only with positive applied potential.

#### Understanding the phenomenon

To understand the mechanism of formation of quartz nanoparticles starting from larger particles, we used first-principles density functional theory calculations to determine the effects of reduced size, electric field, and pH on the processes of cleavage and slip in bulk and a (110) terminated slab of SiO<sub>2</sub>. The  $\alpha$ -SiO<sub>2</sub> structure of quartz belonging to the P3<sub>2</sub>1 (trigonal) space group was used. We chose the (110) plane because it was the one we observed with TEM. Cleavage and slip are two competing processes by which particles can break apart. We define bulk as meaning that the crystal has periodicity along all three directions. We define slab as the breaking of periodicity along the *c* axis, exposing the (110) surface. Cleavage across the (010) plane was introduced by subjecting the crystal to uniaxial tensile strain localized at a single (010) plane (by increasing the separation along the *b* direction) to create two separate constituents (Fig. 3A). We estimated the cleavage energy (two times the surface energy) as the difference between the total energy ( $E_{\text{tot}}$ ) of a crystal cleaved along a specific plane and the total energy of the uncleaved relaxed crystal, which is the energy

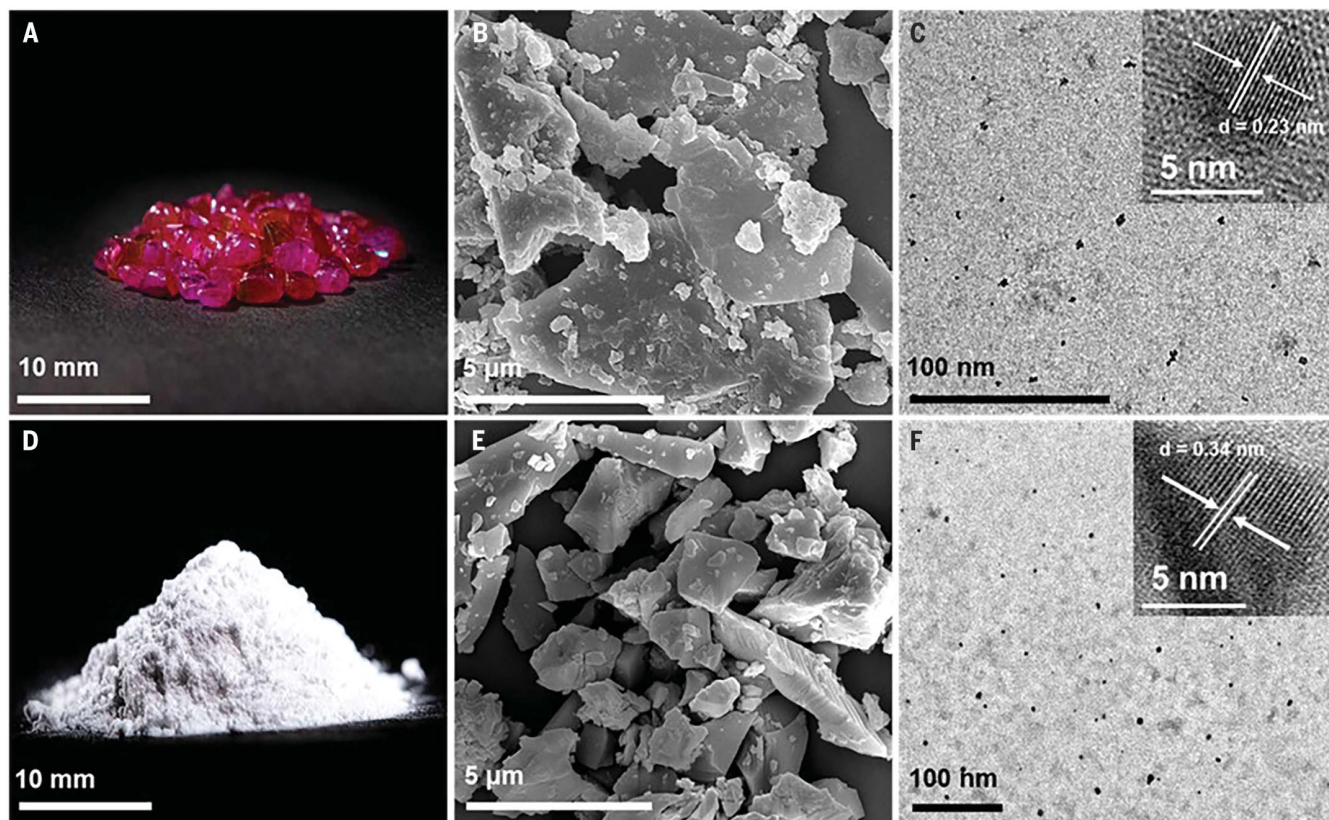


**Fig. 2. Process of disintegration of natural and synthetic alumina in microdroplets.** (A) Photograph of natural ruby. (B) FESEM image of ground and separated natural ruby before electrospray. (C) TEM image of natural ruby after electrospray at optimized conditions. The inset shows a high-resolution image of a particle. The plane marked is (110). (D) Photograph of fused alumina powder. (E) FESEM image of ground and separated fused alumina before electrospray. (F) TEM image of fused alumina after electrospray at optimized conditions. The inset shows a high-resolution image of a particle. The plane marked is (012) of  $\alpha$ -alumina. In (B) and (E), some smaller particles are observed to be attached to the micron-scale particles naturally.

scale relevant to brittle fracture. During the cleavage of bulk and slab  $\text{SiO}_2$ , the energy of cleavage saturates as the separation between surfaces of cleaved parts (Fig. 3B) grows beyond 6 Å. The cleavage energies of the slab are notably lower than that of the bulk, which indicates increased ease in brittle cleavage with reduction in dimension. Consequently, nanocrystals of  $\text{SiO}_2$  are more susceptible to fracture than its bulk form. Cleavage of a slab results in the formation of edges in addition to surfaces, and we note surface and edge reconstruction with concave-convex shapes in cleaved slab with lattice constant  $b = 10 \text{ \AA}$ , where cleavage energy saturates, in contrast to its absence in the cleaved surface of bulk (Fig. 3, C and D).

We examined the competing deformation instability of bulk and slab  $\text{SiO}_2$ . This insta-

bility leads to the formation of a stacking fault on the (010) plane, which is achieved with slip localized at a single (010) plane. To accomplish this, we transformed the unit cell vector  $\bar{v}$  to yield the generalized stacking fault vector,  $\bar{b} \rightarrow \bar{b}_0 + (x, 0, z)$ , where  $\bar{b}$  is the periodic cell vector and  $x, z \in [0, 1]$  are the fractional coordinates (see Fig. 4A). For better understanding, the formation of slip is illustrated in fig. S6. Stacking faults are locally stable at  $(x, z) = (0, 0.5), (0.5, 0)$ , and  $(0.5, 0.5)$  slip configurations, and their energies relative to the reference structure  $(x, z) = (0, 0)$  are used to estimate stacking fault energies (SFEs):

$$\frac{E_{\text{slip}}(x, z) - E_{\text{slip}}(0, 0)}{A}$$

In this equation,  $A = ad$ , where  $a$  is the cell vector and  $d$  is the thickness of the slab. Negative SFEs of the  $(0, 0.5)$  and  $(0.5, 0.5)$  slips in the slab of  $\text{SiO}_2$  mean spontaneous formation of extended stacking faults (table S1). This contrasts with the stacking faults in bulk  $\text{SiO}_2$ , which have positive energies as expected, implying formation of finite-sized stacking faulted regions bordered by partial dislocations (table S1). Thus, both the processes (cleavage and stacking fault formation) are energetically more favorable in the slab than in the bulk. The stability (negative SFE) of the stacking fault in the slab is linked with the creation of a step (relaxed structures reveal shear deformations or steps along the  $b$  direction) (Fig. 4, B and C) and associated reconstruction blunting the fault edges at the surface. Our results

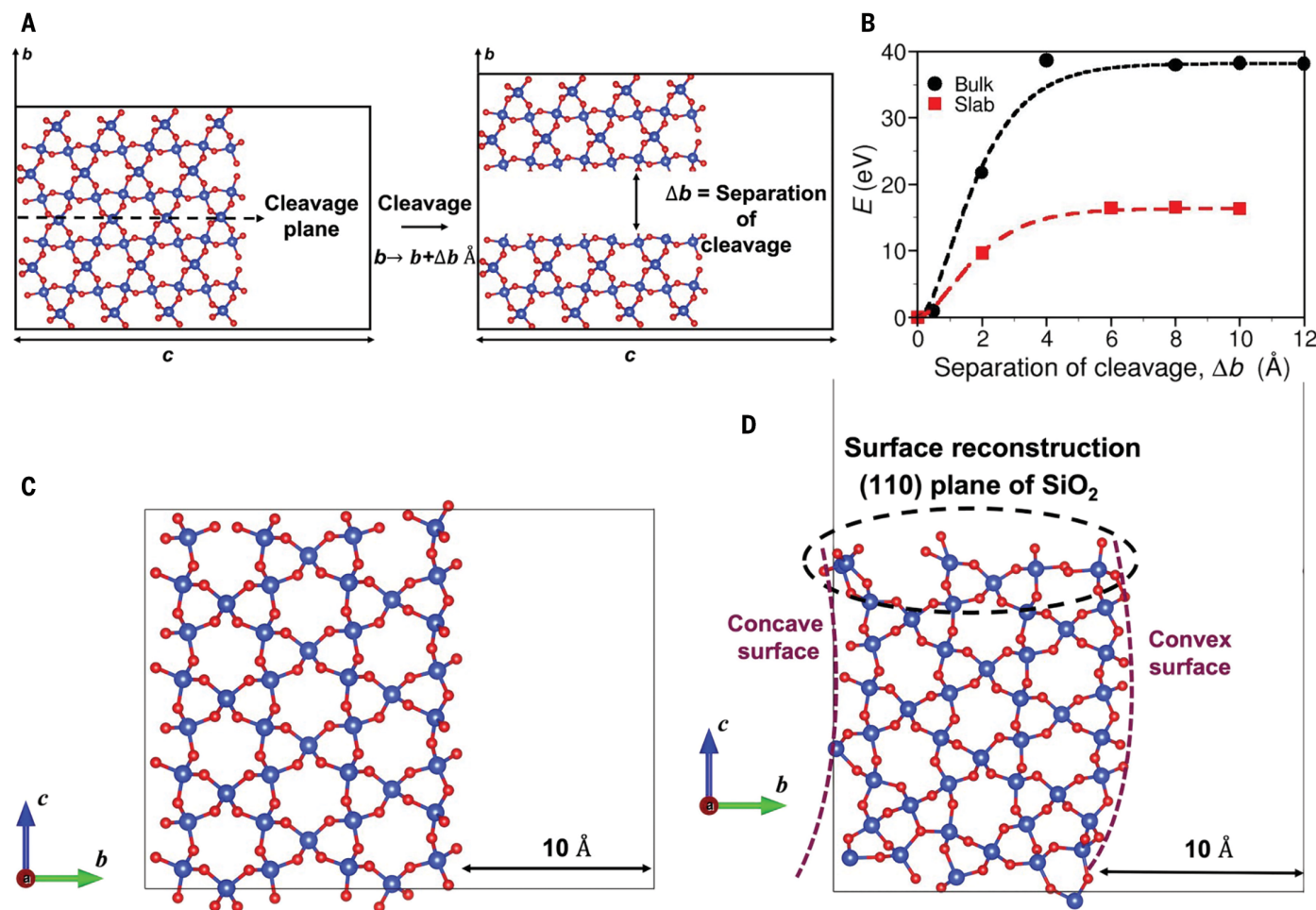


**Fig. 3. The process of cleavage and surface reconstruction visualized with first-principles simulations.** (A) Schematic of the (110) terminated slab of  $\text{SiO}_2$  (left) acted on by uniaxial tensile strain (along the  $b$  axis), resulting in two cleaved surfaces (right). The distance,  $\Delta b$  is a measure of separation of the cleaved surfaces, which is composed of vacuum. (B) The relaxed energies of bulk and slab of  $\text{SiO}_2$  as a function of separation. The energy surface is constructed using the energy functional form,  $E_\infty - E_\infty(1+x)e^{-x}$ , where  $E_\infty$  is the energy of the system in which the cleaved crystals are separated by infinite distance and  $x = \Delta b/l$  (where  $l$

is the length scale in this system) for the relaxed structures as a function of separation. The cleavage energies of slab are lower than that of bulk, indicating that nanoscale crystals of  $\text{SiO}_2$  are much easier to break than the bulk. (C and D) Optimized structures of the (110) surface of (C) bulk [black data in (B)] and (D) slab  $\text{SiO}_2$  [red data in (B)] with a cleavage thickness of 10 Å. We observed concave and convex deformations in the slab. However, no such deformation was seen in the bulk structure. In addition, surface and edge reconstructions were also observed in slab- $\text{SiO}_2$  upon cleavage. Silicon atoms are shown in blue, and oxygen atoms are in red.

show that slip is the primary mechanism that drives the possible formation of nanoparticles in SiO<sub>2</sub>.

Our first-principles analysis of the processes of cleavage and slip in bulk and (001) terminated slab (an alternative plane) of  $\text{SiO}_2$  revealed that the mechanisms of nanocrystal formation in  $\text{SiO}_2$  are not very sensitive to the specific choice of surface (tables S2 and S3). To understand the process of the disintegration of alumina, we simulated the cleavage and slip of a (001) terminated slab of  $\alpha\text{-Al}_2\text{O}_3$ , which has the corundum structure ( $\text{R}\bar{3}\text{c}$ space group) as in silica. The results presented in tables S4 and S5 suggest that its fragmentation to form nanocrystals is indeed driven by the mechanism of slip, similar to silica.

We next investigated the effects of hydrogen (H) atoms on the structure and energies of stacking faults in the (0, 0.5) and (0.5, 0.5) slip configurations. We used H atoms to model protons, which are known to be present in microdroplets, because simulations of a charged system within periodic boundary conditions need to be compensated with opposite charge. Upon addition of a H atom to the structure with slip vector  $(x, z) = (0.5, 0.5)$ , the SFE remained negative. In addition, an H atom is found to destabilize the (0, 0.5) slip system (table S6). Compared with the (0, 0.5) stacking fault structure without an H atom (fig. S7A), substantial local structural distortions arise with H at the sites near the interacting H atom (fig. S7B). Further, interaction with two H atoms results in the formation of silicate fragments or the chipping away of silicate, suggesting that the H atom facilitates fragmentation of a natural mineral such as quartz in microdroplets (fig. S7C). Application of an electric field, as is typical in electrospray experiments ( $E = 10^8$  V/m along the  $c$  axis in Fig. 4) improves the stability of (0, 0.5) and (0.5, 0) stacking faults in  $\text{SiO}_2$  (table S6).

Our theoretical analysis of mechanical instabilities in bulk and a nanoslab of SiO<sub>2</sub> (cleavage and slip in response to localized uniaxial and shear strains, respectively) suggests that the stacking faults and resulting steps at the surface of SiO<sub>2</sub> may occur in the initial stage of fragmentation into nanoparticles, and the interactions with H atoms and electric field enhance this process, leading to the formation of silicate fragments. Because the cleavage energies decrease substantially with a reduction in dimension, namely, from bulk to slab, we expected fragmentation to follow readily, with possible nucleation at the steps, or the sites of chemical interaction with protons. In addition to the stacking faults and resulting steps, several aspects of the microdroplet environment can drive the fragmentation process. Chemical reaction rate constants can be increased by a factor of more than 10<sup>6</sup> in such confinement (2). Several factors such

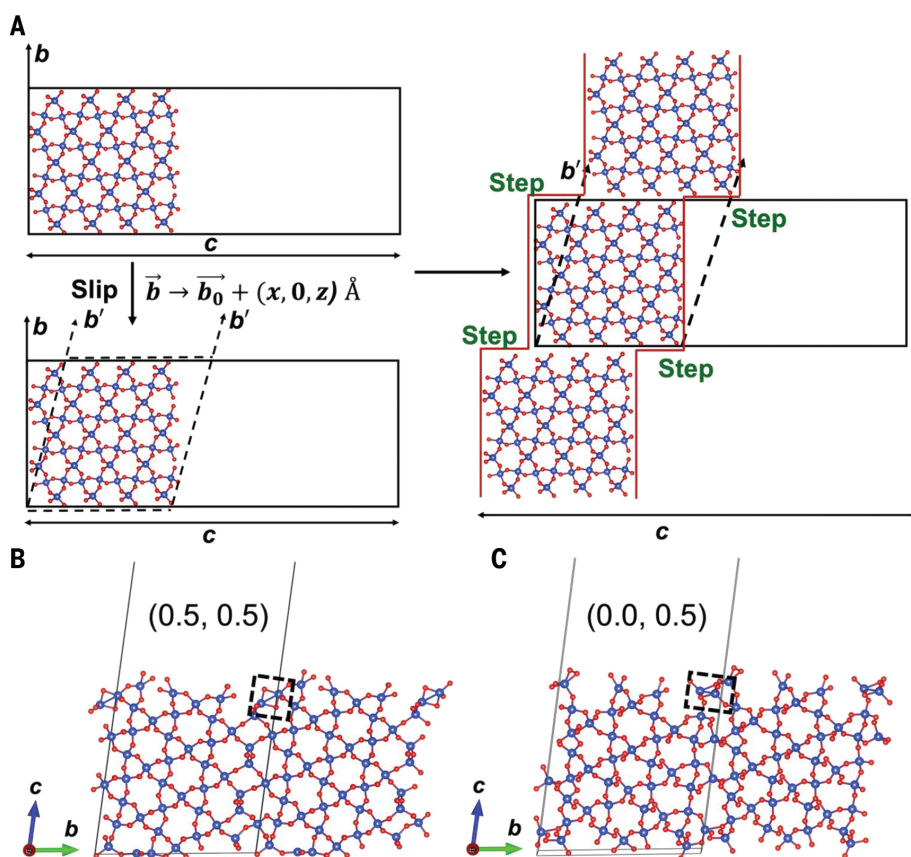


**Fig. 4. Stacking fault or slip localized at a (010) plane.** (A) Schematic of the (110) terminated slab of  $\text{SiO}_2$  acted on by localized shear strain (slip) on (010) plane introduced through a generalized stacking fault vector  $\vec{f} = x\vec{a} + z\vec{c}$ , where  $\vec{a}$  and  $\vec{c}$  are periodic cell vectors and  $(x, z \in [0, 1])$  are the fractional coordinates. (B and C) Relaxed stacking fault structures with (B)  $(x, z) = (0.5, 0.5)$  and (C)  $(x, z) = (0, 0.5)$ . The stacking fault or slip on the (010) plane is introduced by tilting  $\vec{b}$  (dashed boxes). Two-unit cells along the  $\vec{b}$  direction are shown for clearer visualization. Silicon atoms are shown in blue, and oxygen atoms are in red.

as pH (6), reactive species such as radicals (7), their surface segregation, strong electric field at the interface (8), and others are likely to contribute additionally to these effects, and some of these may accelerate the process.

## Formation of silicates in microdroplets

To test the hypothesis of formation of silicates by microdroplet-induced fragmentation, we electrosprayed 5 mg of silica in 50 ml of water at the optimized conditions on an aluminum substrate. The product was collected, redispersed in water, and centrifuged at 10,000 rpm to remove any larger particles. The upper layer was used for mass spectrometric measurements. In the negative ion mass spectrum of the deposited silica (Fig. 5A), the peaks appeared at mass/charge ratios ( $m/z$ ) 60.9, 76.9, 94.9, 154.9, and 172.9. This spectrum was compared with that of 200  $\mu\text{M}$  standard sodium silicate solution at pH 8.5 (Fig. 5B). We observed peaks at  $m/z$  60.9, 76.9, 94.9, 154.9, and 172.9 due to  $[\text{SiO}_2\text{H}]^-$ ,  $[\text{SiO}_3\text{H}]^-$ ,  $[\text{SiO}_3\text{H}_2\text{O}]^-$ ,  $[\text{Si}_2\text{O}_5\text{H}_2]^-$ , and  $[\text{Si}_3\text{O}_6\text{H}_3\cdot\text{H}_2\text{O}]^-$ .

respectively. In addition, we observed peaks at higher masses at  $m/z$  194.9 [ $\text{Si}_2\text{O}_6\text{H}_2\text{Na} \cdot \text{H}_2\text{O}$ ]<sup>-</sup>,  $m/z$  212.9 [ $\text{Si}_2\text{O}_6\text{H}_2\text{Na} \cdot 2\text{H}_2\text{O}$ ]<sup>-</sup>, and  $m/z$  232.9 [ $\text{Si}_3\text{O}_9\text{H}_5$ ]<sup>-</sup>. We did not observe sodium adduct peaks of the standard sodium silicate in the spectrum of deposited silica. Tandem mass spectrometric analysis for sodium silicate (fig. S8) and deposited silica (Fig. 5, C and D) showed the expected features. Two peaks at  $m/z$  94.9 and 172.9 showed the loss of water, confirming the formation of [ $\text{SiO}_3\text{H}\cdot\text{H}_2\text{O}$ ]<sup>-</sup> and [ $\text{Si}_2\text{O}_6\text{H}_3 \cdot \text{H}_2\text{O}$ ]<sup>-</sup> complexes.

## Plausible mechanisms

With respect to the energy needed for such processes, our calculations suggest that physical effects in microdroplets are particularly important. Microdroplet convection and shock waves that produce pressures in the megabar range (9) are likely in droplets, which could trigger such effects. We suggest that the observed phenomenon is critically influenced by the following factors: (i) Droplet fission occurs due to Coulomb repulsion. We know from the

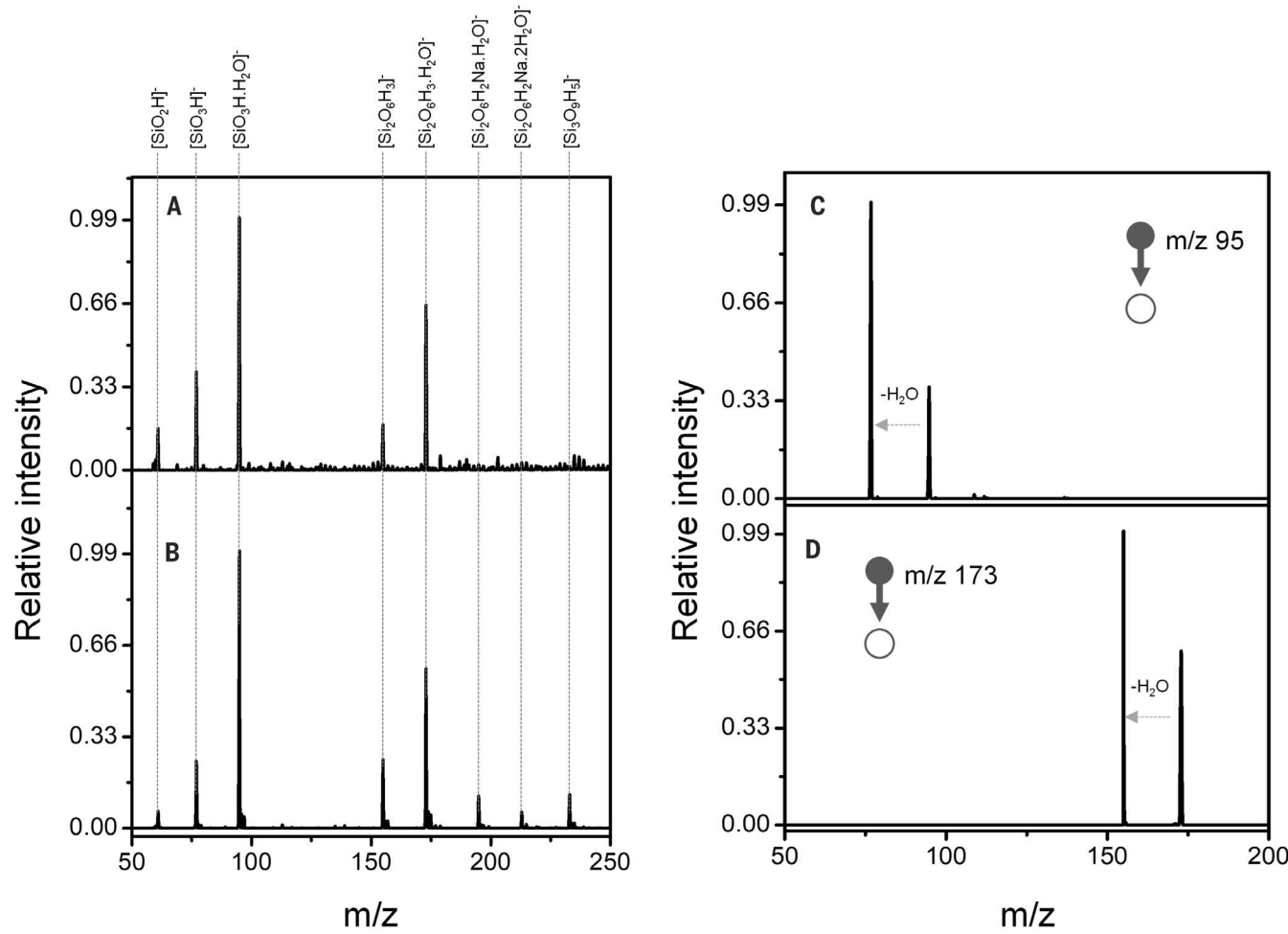


**Fig. 5. Mass spectra of silica samples.** (A and B) Full-range negative ion mass spectrum of (A) the deposited silica showing the peaks due to silicates compared with that of (B) standard sodium silicate. (C and D) Tandem mass spectra of (C)  $[\text{SiO}_3\text{H}_2\text{O}]^-$  and (D)  $[\text{Si}_2\text{O}_6\text{H}_3\text{H}_2\text{O}]^-$ , showing water loss during fragmentation.

literature that the droplets produced at low flow rates (typically  $\sim 5 \mu\text{l}/\text{min}$ ) have a narrow distribution of sizes, with the most abundant radius in the range of  $1.5 \mu\text{m}$ . Such an electrospray droplet was shown to have an electric charge of  $\sim 10^{-14} \text{ C}$ , which corresponds to  $\sim 60,000$  singly charged ions (10). In our case, the droplet sizes are larger, in the range of approximately tens of micrometers (11); produced at a flow rate of  $0.5 \text{ ml}/\text{hour}$ , that is,  $8.3 \mu\text{l}/\text{min}$ ; and large enough to accommodate the parent particles. The droplet size reduces along the flight path, which results in the explosion of the droplets. This explosion produces smaller droplets that experience larger stresses (9), leading to the breakage of particles. (ii) Erosion of the quartz particles in the charged droplets and solubility of quartz in water (6 parts per million at  $25^\circ\text{C}$ ) together bring  $\text{SiO}_2$  species into the solution. We tested the possible effect of enhanced acidity in microdroplets on the mineral particles in a separate experiment by electrospraying pure water on the parent minerals for 4 hours (fig. S9). We saw surface roughening in this experiment, although the changes

are much less pronounced than those shown in Fig. 1. The reactive species at the droplet-air interface may play an important role in these events. (iii) The dissolution and reprecipitation of silica particles may occur in microdroplets. The solubility of quartz in water is influenced by factors such as electrostatic forces, hydration-induced ionization, pH, and Laplace pressure. The interaction between charged silica particles and water droplets is substantial, resulting in the formation of reactive species. We observed the formation of silicate ions during the process (Fig. 5). These ions may reprecipitate under specific conditions. Charged microdroplets can modify surface chemistry, promoting dissolution that leads to nano-sized silica particles. However, these chemical events may occur slowly and therefore may not fully explain the phenomenon of formation of crystalline nanoparticles. (iv) The  $\text{H}_2\text{O}$  radical cation present in the microdroplets (7) can also contribute to the observed phenomenon. To probe this possibility, we analyzed the formation of nanoparticles from silica by simulating it as a charged system. The  $\text{H}_2\text{O}$  radical cation

present in the microdroplets may pull out electrons from silica, and we have simulated the process by removing an electron from the system and adding a compensating jellium background to remove electrostatic divergence of the charged periodic system. Our results confirm that the generalized SFE of slip along the (010) plane is negative [see (0.5, 0.5) slip configuration of the  $\text{SiO}_2$  slab in table S7]. (v) The nanoparticles that form may catalyze the fission of microdroplets. This assumption is supported by a study in which it was shown theoretically that nanoparticles actively fragment droplets (12). Accelerated droplet fission further accelerates the particle disintegration. We present a schematic of the fragmentation process in fig. S10.

Atmospheric water droplets, such as clouds and fog, can acquire charges not only because of the ionic species present inside them but also because of contact electrification (13). These charges on naturally occurring droplets cannot be ignored. As we have demonstrated, under the right conditions, electrosprayed microdroplets can break hard particles, including

complex minerals, and the potential of naturally occurring atmospheric droplets to do the same needs to be explored. If this process does happen, it would be important for weathering and the production of natural nanoparticles (1). Soil forms through rock weathering, a process that involves multiple factors, and it takes 200 to 400 years to yield 1 cm of it, composed of varied particle sizes. Our study highlights the role of charged microdroplets of water in unprecedented weathering, which, to our knowledge, had not yet been explored. Disintegration of minerals makes nascent surfaces, which may participate in catalysis that leads to new chemical transformations in droplets in the presence of reactive species. “Microdroplet showers” composed of nanoparticles and molecules falling on Earth may be of importance to the chemical and biological evolution of the planet.

#### REFERENCES AND NOTES

- M. F. Hochella Jr. et al., *Science* **363**, eaau8299 (2019).
- Z. Wei, Y. Li, R. G. Cooks, X. Yan, *Annu. Rev. Phys. Chem.* **71**, 31–51 (2020).
- J. K. Lee, S. Kim, H. G. Nam, R. N. Zare, *Proc. Natl. Acad. Sci. U.S.A.* **112**, 3898–3903 (2015).
- A. Wortmann et al., *J. Am. Soc. Mass Spectrom.* **18**, 385–393 (2007).
- D. Sarkar et al., *Adv. Mater. Interfaces* **5**, 1800667 (2018).
- H. Wei et al., *Proc. Natl. Acad. Sci. U.S.A.* **115**, 7272–7277 (2018).
- L. Qiu, N. M. Morato, K.-H. Huang, R. G. Cooks, *Front Chem.* **10**, 903774 (2022).
- D. Zhang, X. Yuan, C. Gong, X. Zhang, *J. Am. Chem. Soc.* **144**, 16184–16190 (2022).
- M. S. Krivokorytov et al., *Phys. Rev. E* **95**, 031101 (2017).
- S. Banerjee, S. Mazumdar, *Int. J. Anal. Chem.* **2012**, 282574 (2012).
- P. Basuri et al., *Chem. Sci.* **13**, 13321–13329 (2022).
- F. Sicard, J. Toro-Mendoza, A. Striolo, *ACS Nano* **13**, 9498–9503 (2019).
- Z. Tang, S. Lin, Z. L. Wang, *Adv. Mater.* **33**, e2102886 (2021).

#### ACKNOWLEDGMENTS

**Funding:** We acknowledge financial support from the Department of Science and Technology, government of India. We thank M.S.R. Rao for allowing access to his powder x-ray diffraction facility. We thank S. Manna for help with the Raman measurements. B.K.S. thanks the University Grant Commission (UGC) for a research fellowship. P.B. and A.N. thank Indian Institute of Technology (IIT) Madras for their fellowships. K.D. thanks Jawaharlal Nehru Centre for Advanced Scientific Research (JNCASR) for her fellowship. T.P. acknowledges funding from the Centre of Excellence on Molecular Materials and

Functions under the Institution of Eminence Scheme of IIT Madras. T.P. and U.V.W. acknowledge support from JC Bose National Fellowships.

**Author contributions:** T.P. proposed the problem and suggested necessary experiments. B.K.S. performed the synthesis and characterization. K.D. and U.V.W. conducted the computational work. P.B. participated in designing the experimental setup. A.N. performed scanning electron microscopy. T.P. supervised the research. All authors discussed the results and contributed to the writing of the manuscript.

**Competing interests:** T.P., B.K.S., P.B., and A.N. are the authors of two pending patent applications: nos. 202241038282 and PCT/IN2023/050649. The authors declare no other competing interests. **Data and materials availability:** All relevant data are provided in this paper or the supplementary materials. **License information:** Copyright © 2024 the authors, some rights reserved; exclusive licensee American Association for the Advancement of Science. No claim to original US government works. <https://www.science.org/about/science-licenses-journal-article-reuse>

#### SUPPLEMENTARY MATERIALS

[science.org/doi/10.1126/science.adl3364](https://science.org/doi/10.1126/science.adl3364)

Materials and Methods

Supplementary Text

Figs. S1 to S10

Tables S1 to S7

References (14–17)

Movie S1

Submitted 12 October 2023; accepted 8 April 2024  
10.1126/science.adl3364